

Supplementary Information

Unveiling the corrosion mechanism of 3-nitro-1,2,4-triazol-5-one (NTO) toward mild steel from *ab initio* Molecular Dynamics: How “nitro-to-amino” reaction matters

Ziyang Guo^a, Liyuan Qin^a, Shuai Zhao^{*c}, Deqiu Wang^g, Xijuan Lv^c, Yujie Qiang^f, Wei Guo^{*cde}, Qinghai Shu^{*ab}, Y. Yao^{cde}

^a School of Materials Science and Engineering, Beijing Institute of Technology, Beijing 100081, China

^b Guangxi Energetic Materials and Damage Technology Engineering Research Center, Guilin 541003, China

^c Key Lab of Advanced Optoelectronic Quantum Architecture and Measurement (MOE), Beijing Key Lab of Nanophotonics & Ultrafine Optoelectronic Systems, School of Physics, Beijing Institute of Technology, Beijing 100081, China

^d State Key Laboratory of Explosion Science and Technology, Beijing Institute of Technology, Beijing 100081, China

^e Frontiers Science Center for High Energy Material (MOE), Beijing Institute of Technology, Beijing 100081, China

^f National Center for Materials Service Safety, University of Science and Technology Beijing, Beijing 100083, China

^g Gansu Yinguang Juyin Chemical Co., Ltd., Baiyin 730900, China

Supplement Note S1.

Quantum chemical calculation in this work was implemented by using Gaussian 09 software to investigate the geometries and harmonic vibrational frequencies of NTO [1]. Neutral and anionic NTO molecules were optimized using B3LYP method with 6-311++G (d, p) basis set at density functional theory (DFT) level [2]. The standard equation $\Delta G = \Delta H - T\Delta S$ was employed to calculate the change in Gibbs free energy of NTO and its anion in aqueous solution at 298.15 K. Afterward, the related parameters, including the energy of the highest occupied molecular orbital (E_{HOMO}) and the energy of the lowest occupied molecular orbital (E_{LOMO}), electrostatic potential (ESP) were attained.

Supplement Note S2.

The initial NTO-H₂O system (1 NTO with 83 H₂O molecules) was constructed using the PACKMOL program [3]. Subsequently, the structure underwent a pre-equilibration phase of 1 ns simulation with a timestep of 1 fs, employing the COMPASS II force field and utilizing the NVT ensemble within the Forcite module [4]. Following the pre-equilibration phase, the structure was subjected to a 5 ps equilibration period in the AIMD simulations. The equilibration was conducted at a finite temperature of 330 K, employing a timestep of 1 fs and utilizing the NVT ensemble. Note that the initial configuration was pre-optimized before starting the constrained MD simulation with “slow growth” approach [5].

In this enhanced sampling method (“slow growth” method), the value of the reaction coordinate (label as ξ) is linearly changed from the characteristic value for the initial state (ξ_1) to that for the final state (ξ_2). The formula for calculating the free energy difference by integrating along the initial and final state reaction coordinates is as follows [6]:

$$W_{\xi_2} - W_{\xi_1} = \int_{\xi_1}^{\xi_2} d\xi \frac{dW}{d\xi} = \int_{\xi_1}^{\xi_2} d\xi \left\langle \frac{\partial H}{\partial \xi} \right\rangle_{\xi} \quad (1)$$

where the free energy gradient $\frac{dW}{d\xi}$ can be computed from the ensemble averaged derivative of Hamiltonian (H) over the variable ε . The integrand $\frac{dW}{d\xi}$ or $\left\langle \frac{\partial H}{\partial \xi} \right\rangle_{\xi}$ is also called the mean force, and the free energy can be considered as the potential of mean force. The mean force can be obtained as below:

$$\frac{dW}{d\xi} = \frac{\langle Z^{-1/2}(-\lambda + kTG) \rangle_{\xi}}{\langle Z^{-1/2} \rangle_{\xi}} \quad (2)$$

$$Z = \sum_i \frac{1}{m_i} \left(\frac{\partial \xi}{\partial r_i} \right)^2 \quad (3)$$

$$G = Z^{-1/2} \sum_{ij} \frac{1}{m_i m_j} \frac{\partial \xi}{\partial r_i} \frac{\partial \xi}{\partial r_j} \frac{\partial \xi}{\partial r_j} \quad (4)$$

λ is the Lagrange multiplier to constrain the reaction coordinate, modifying the Lagrangian to be:

$$L'(r, p, \xi) = L(r, p) + \lambda[\xi(r) - \xi] \quad (5)$$

The λ can be determined using SHAKE algorithm [7]. In addition to manually choosing a few ε values along the reaction path, it is also possible to automate the variation of ξ by applying a constant speed $\dot{\xi}$. It can be seen as follows [8]:

$$W_{\xi_2} - W_{\xi_1} = \int_{\xi_1}^{\xi_2} \left\langle \frac{\partial H}{\partial \xi} \right\rangle_{\xi} d\varepsilon = \lim_{\xi \rightarrow 0} \int_{\xi_1}^{\xi_2} \frac{\partial H}{\partial \xi} \dot{\xi} dt \quad (6)$$

The work $W_{\xi_2} - W_{\xi_1}$ corresponds to the free energy difference between the final and initial state [9].

The radial distribution function (RDF) is defined as:

$$g_{N-O}(r) = \frac{\bar{V}}{4\pi r^2 N_O} \frac{dn_{N-O}(r)}{dr} \quad (7)$$

where \bar{V} is the average cell volume, N_O is the total number of oxygen atom, $dn_{N-O}(r)$ is the number of oxygen atom in the elementary volume separated from nitrogen atom

between r and $r + dr$.

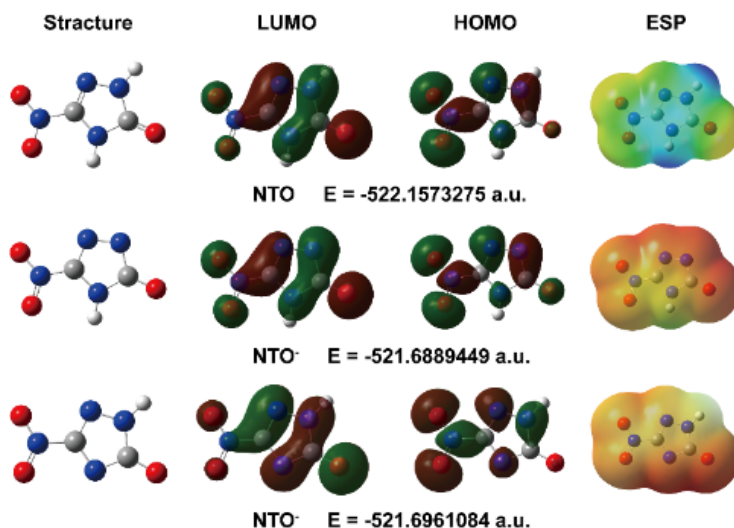


Fig. S1. The optimized geometry configuration, LUMO, HOMO, ESP maps of neutral and deprotonated NTO molecule.

For the two NTO anions in **Fig. S1**, compared with the NTO anion that removes H1, the configuration after hydrogen dissociation at the N4 site has a lower relative energy, implying that NTO is more inclined to form the latter in aqueous solution. Furthermore, the LUMO and HOMO distributed over entire molecule, which suggested a flat adsorption configuration of the NTO and NTO anion on Fe substrate [10]. Especially, in the ESP maps, it could be observed that the orange (negative) regions with nucleophilic reactivity distributed on the nitro, carbonyl and N1 or N4 side, whereas the blue (positive) regions associated with electrophilic reactivity were mainly presented on protons. These areas are easily available to interact with Fe surface [11].

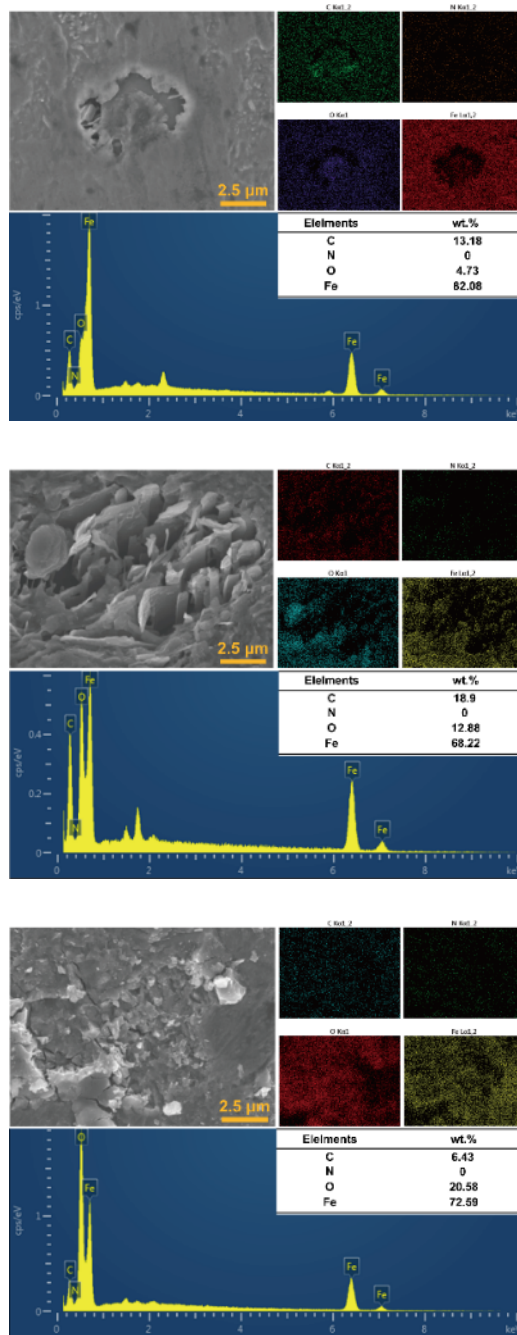


Fig. S2. Elemental mapping images and energy dispersive X-ray spectroscopy of the surface after 10-, 20- and 30-days corrosion experiments. 10 to 30 days from top to bottom.

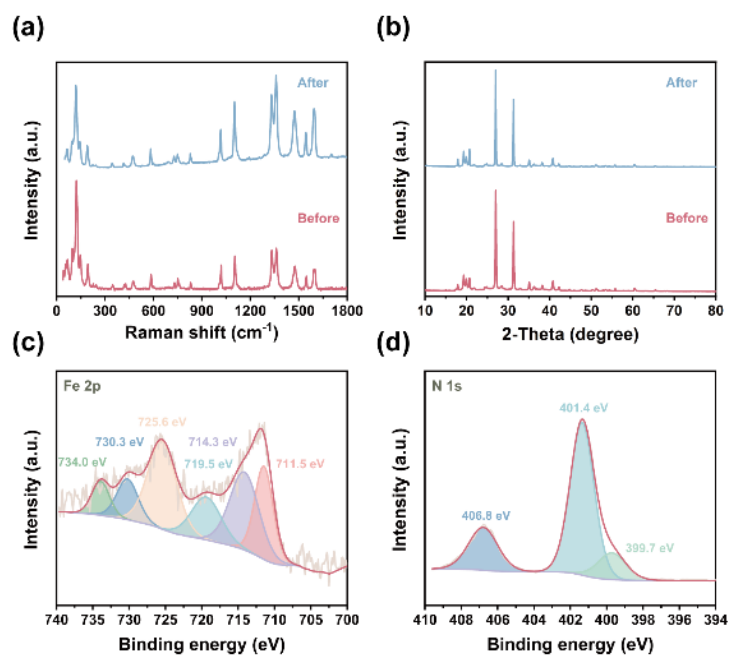


Fig. S3. (a) Raman spectra of NTO before and after corrosion experiment, (b) XRD pattern of NTO after corrosion experiment, (c) the high-resolution XPS spectra of Fe 2p and (d) N 1s in NTO after 30 days corrosion experiment.

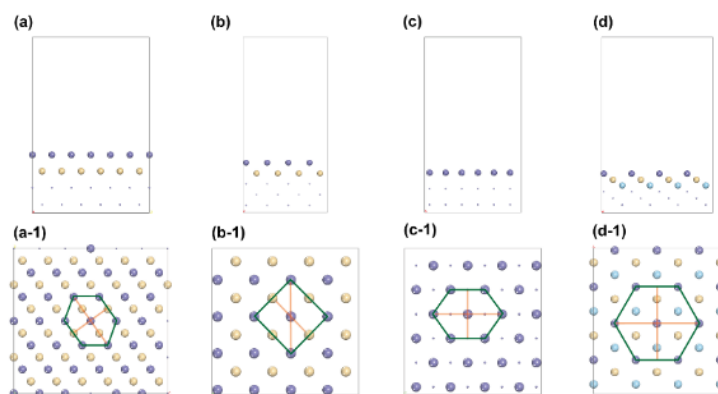


Fig. S4. (a, a-1) Structures of the four-layer Fe(110), (b, b-1) five-layer Fe(100), (c, c-1) three-layer Fe(110), and (d, d-1) six-layer Fe(111). Dark blue, yellow and sky blue represent the first, second and third layers of atoms, respectively. The green boundary is a selected basic adsorption unit, and the orange line describes the initial position of the NTO molecule.

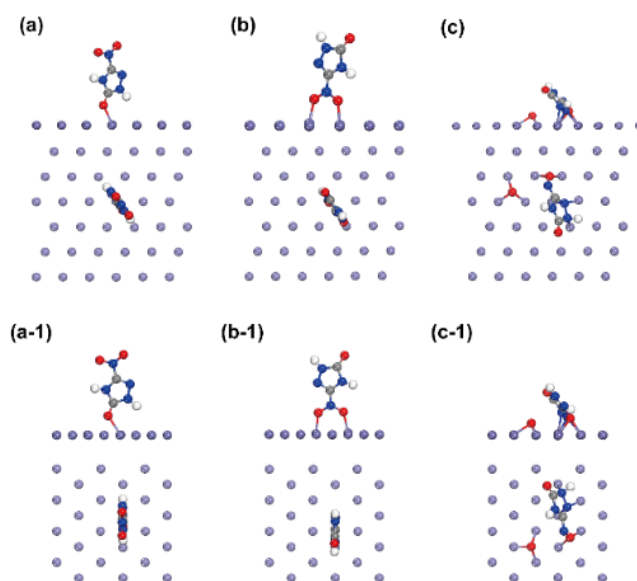


Fig. S5. Comparison of adsorption configurations of NTO on Fe(110) with four layers (144 atoms, top) and three layers (72 atoms, bottom). (a, a-1) nfc-Fe(110), (b, b-1) nfc-Fe(110), (c, c-1) nfp-Fe(110). Carbon, hydrogen, oxygen, nitrogen and iron atoms are depicted as grey, white, red, blue and purple, respectively.

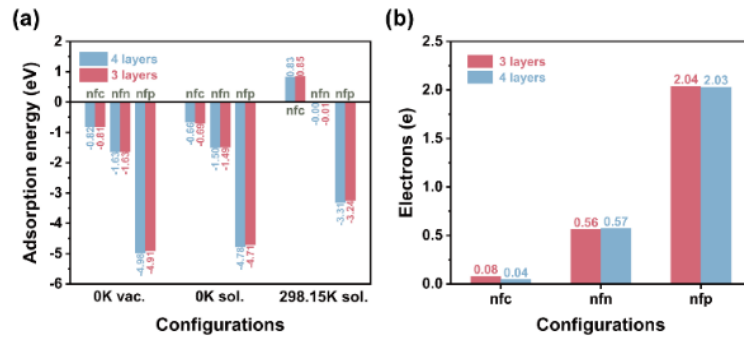


Fig. S6. Comparison of (a) adsorption energy and (b) Bader charge of NTO on Fe(110) with four layers (144 atoms) and three layers (72 atoms), a positive value represents NTO gains electrons.

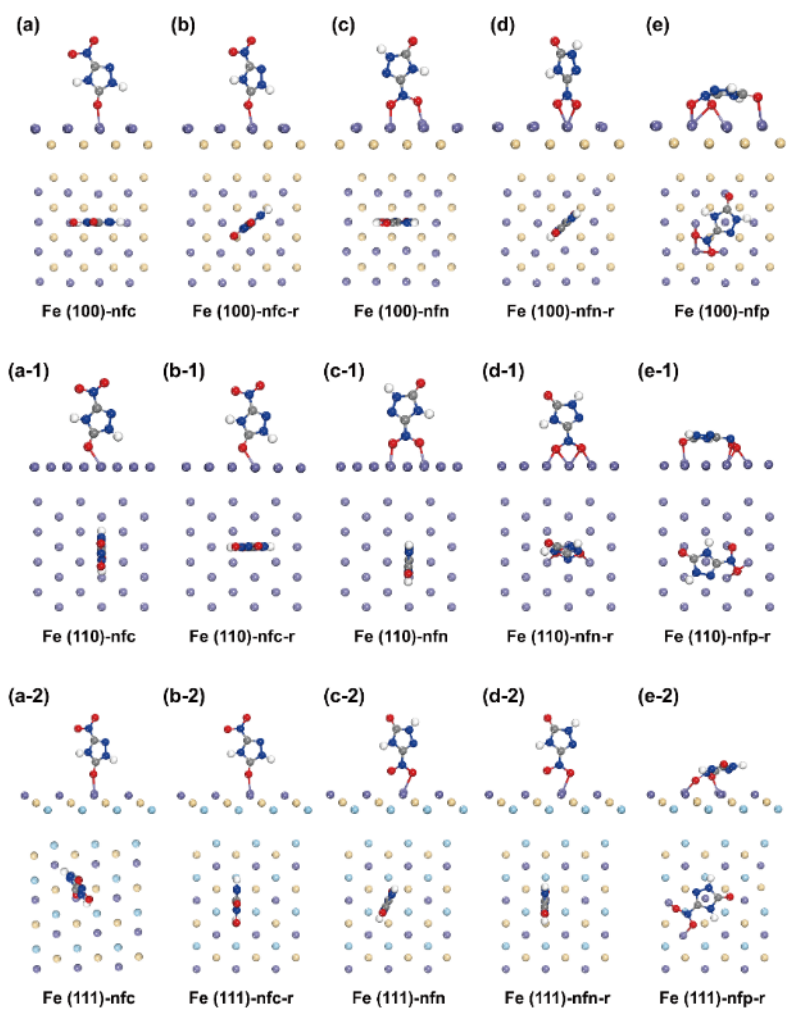


Fig. S7. The various adsorption configurations of NTO on different surfaces, (a-e) Fe(100), ((a-1)-(e-1)) Fe(110) and ((a-2)-(e-2)) Fe(111), respectively. The first layer of iron is shown in purple, the second and third layers of iron are shown in yellow and sky blue, respectively.

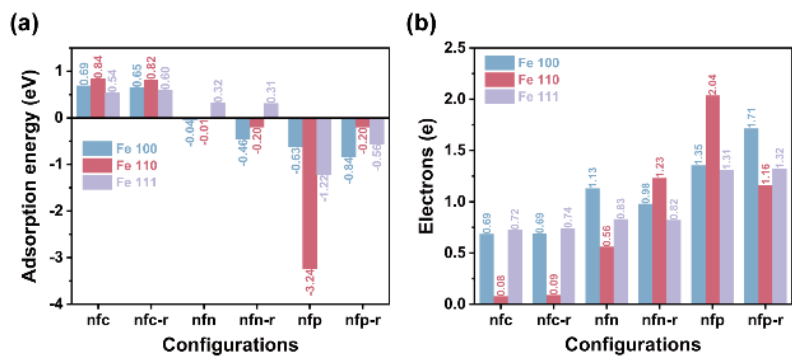


Fig. S8. (a) Adsorption energy and (b) bader charge of NTO on different surfaces, positive values indicate NTO gaining electrons.

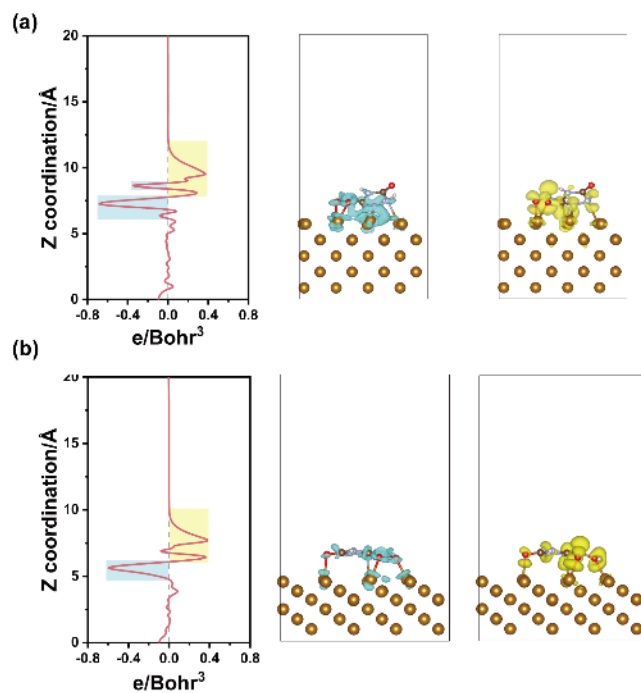


Fig. S9. (a) Z-axis and three-dimensional charge density difference of nfp-r-Fe(100) and (b) nfp-Fe(111). The blue isosurface suggests the decrease of electron density, and the yellow isosurface depicts the increase of electron density ($0.0045 \text{ electrons/\AA}$). Carbon, hydrogen, oxygen and nitrogen atoms are depicted as grey, white, red and blue, respectively.

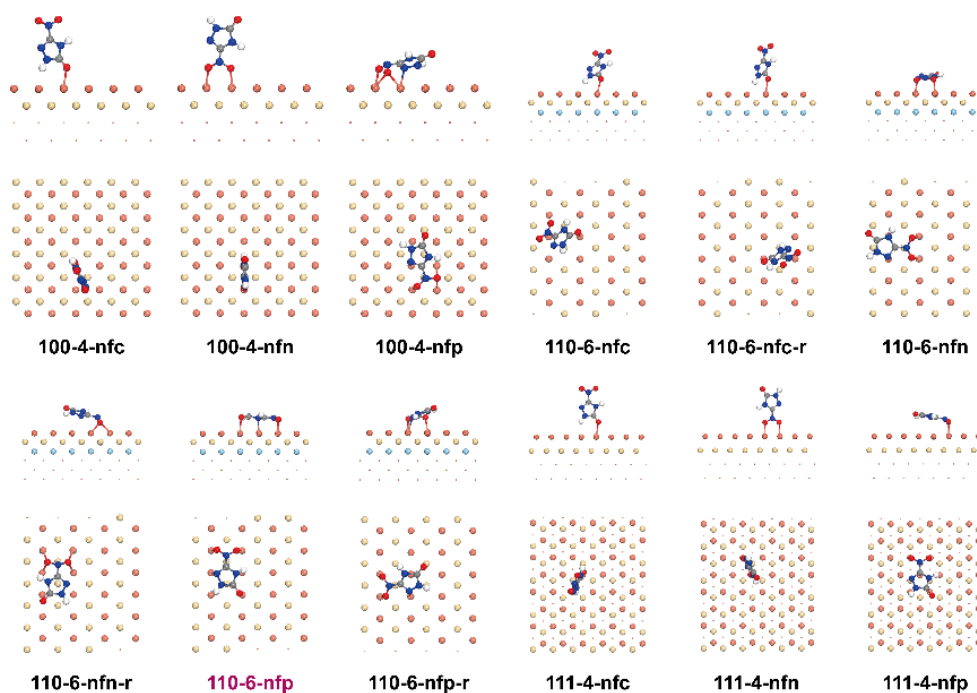


Fig. S10. The various adsorption configurations of NTO on different copper surface, Cu(100), Cu(110) and Cu(111), respectively. Carbon, hydrogen, oxygen and nitrogen atoms are depicted as grey, white, red and blue, respectively. The first layer of Cu is shown in orange, the second and third layers of iron are shown in yellow and sky blue, respectively. The red letter indicates the configuration with the lowest adsorption energy.

To compare the adsorption behavior of NTO on commonly used metal copper (**Fig. S10**), three typical low-index crystal planes of copper were selected as substrates. Among them, the (100) and (111) facets are 4 layers, while the (110) facet is 6 layers, with half of the layers fixed in the calculation to simulate the bulk material. **Fig. S10** shows that NTO has the most stable adsorption configuration when it is adsorbed in parallel on the Cu(110) surface, where copper donates $0.98 |e|$ to NTO. However, the interaction of NTO with the Cu surface is not as strong as that of Fe, which can be attributed to that the electronic arrangement of the outermost layer $3d^{10}$ of Cu is less active than that of Fe $3d^6$. Moreover, the weaker the interaction of NTO on Cu surfaces is also observed in the differential charge density (**Fig. S11(b)**).

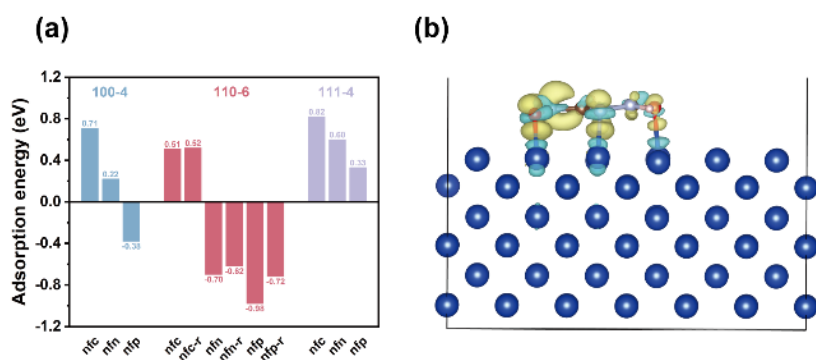


Fig. S11. (a) Adsorption energy of NTO on different copper surface, (b) Charge density difference of the most stable adsorption of NTO on nfp-Cu(110). The blue isosurface suggests the decrease of electron density, and the yellow isosurface depicts the increase of electron density (0.0045 electrons/Å³). Carbon, hydrogen, oxygen, nitrogen, and copper are depicted as grey, white, red, brown, and blue, respectively.

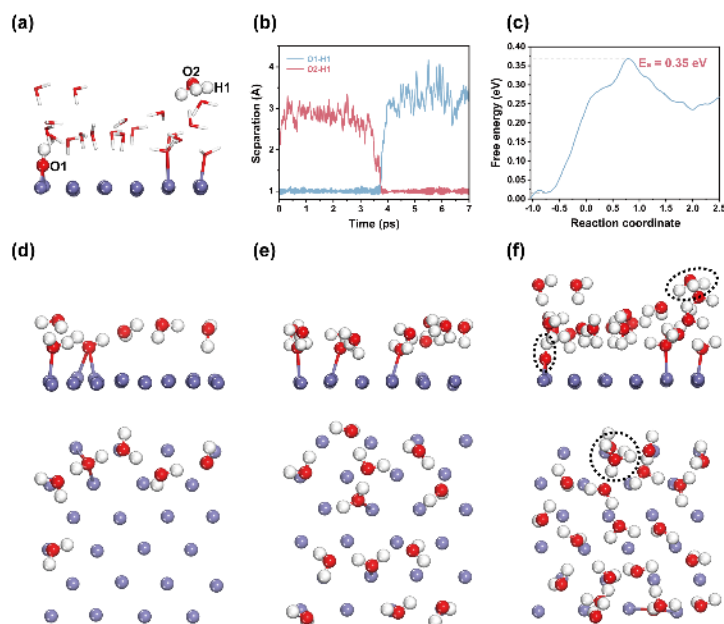


Fig. S12. (a) Selected snapshot of adsorbed 1 ML H₂O on Fe(110) after 20 ps, (b) O1-H1 and O2-H1 pair trajectory within 7 ps simulation, (c) the free energy profile of H₂O dissociation on Fe(110) ($CV = r_{O1-H1} - r_{O2-H1}$). Snapshots of adsorbed water molecules on Fe(110) after a 20 ps AIMD simulation, (d) 0.25 ML, (e) 0.5 ML. (f) 1 ML, respectively. The formed *OH and H₃O⁺ are indicated by dashed circles.

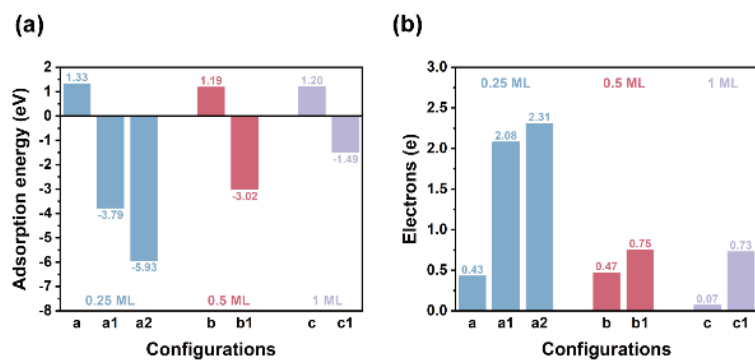


Fig. S13. (a) Adsorption energy of NTO and NTO anion on (a, a1, a2) 0.25 ML, (b, b1) 0.5 ML and (c, c1) 1 ML surface; (b) Bader charge of corresponding to NTO and NTO anion on different surfaces. Where a corresponds to **Fig. 6(a)**, a1 corresponds to **Fig. 6(b)**, a2 corresponds to **Fig. 6(e)**, b corresponds to **Fig. 6(c)**, b1 corresponds to **Fig. 6(f)**, c corresponds to **Fig. 6(d)**, and c1 corresponds to **Fig. 6(g)**, respectively.

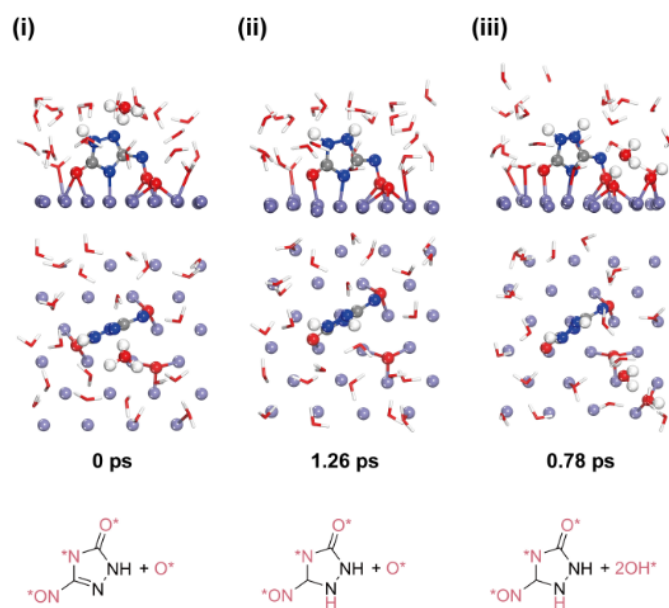


Fig. S14. Selected snapshots of the AIMD trajectory for NTO anion adsorbed on Fe(110) in water at 330 K. (i) $*\text{C}_2\text{HN}_4\text{O}_2 + *O$, (ii) $*\text{C}_2\text{H}_2\text{N}_4\text{O}_2 + *O$, (iii) $*\text{C}_2\text{H}_2\text{N}_4\text{O}_2 + *OH$. The corresponding chemical structure is shown at the bottom of the picture. Some H_2O molecules are hidden for view convenience.

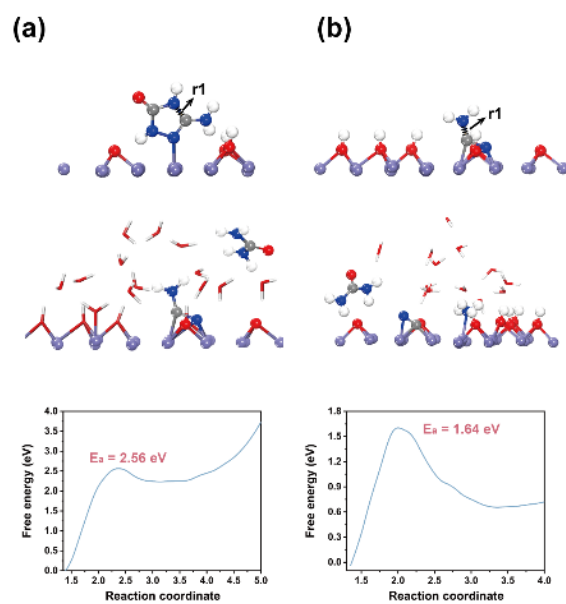
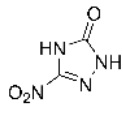
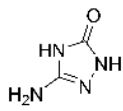


Fig. S15. Free energy profiles of the two reactions at 330 K: (a) $*C_2H_4N_4O \rightarrow *CH_2N_2 + CO(NH_2)_2$ ($CV = -r_1$), (b) $*CH_2N_2 \rightarrow *NH_3 + *CN$ ($CV = -r_1$). The middle figure shows the final state of the enhanced sampling. Some H_2O molecules are hidden for view convenience.

Table S1. The compositions of the mild steel

Elements	C	Cr	Mn	Ni	P	S	Si	Fe
wt.%	0.42-0.50	≤0.25	0.50-0.80	≤0.25	≤0.035	≤0.035	0.17-0.37	balance

Table S2. Selected properties of NTO and ATO [12]

Name	Structure	Molecular weight	pKa	S _w (mg/L)	Log K _{ow}
NTO		130.06	3.76 [13]	16642 [14]	0.21 [15]
ATO		100.08	9.17-17.07 [12]	11000 [12]	N/A

N.A. (not applicable); N/A (not available); pKa (acid dissociation constant); S_w (water solubility); K_{ow} (octanol-water partition coefficient)

Reference:

- [1] Frisch MJ, Trucks GW, Schlegel HB, Scuseria GE, Robb MA, Cheeseman JR, Scalmani G, Barone V, Mennucci B, Petersson GA, Nakatsuji H, Caricato M, Li X, Hratchian HP, Izmaylov AF, Bloino J, Zheng G, Sonnenberg JL, Hada M, Ehara M, Toyota K, Fukuda R, Hasegawa J, Ishida M, Nakajima T, Honda Y, Kitao O, Nakai H, Vreven T, Montgomery Jr JA, Peralta JE, Ogliaro F, Bearpark M, Heyd JJ, Brothers E, Kudin KN, Staroverov VN, Kobayashi R, Normand J, Raghavachari K, Rendell A, Burant JC, Iyengar SS, Tomasi J, Cossi M, Rega N, Millam JM, Klene M, Knox JE, Cross JB, Bakken V, Adamo C, Jaramillo J, Gomperts R, Stratmann RE, Yazyev O, Austin AJ, Cammi R, Pomelli C, Ochterski JW, Martin RL, Morokuma K, Zakrzewski VG, Voth GA, Salvador P, Dannenberg JJ, Dapprich S, Daniels AD, Farkas O, Foresman JB, Ortiz JV, Cioslowski J, Fox DJ (2009) Gaussian 09, Revision D.01. Gaussian Inc., Wallingford.
- [2] J. Wang, M.K. Shukla, Density functional theory investigation on the degradation mechanisms of 3-nitro-1,2,4-triazol-5-one (NTO) in water, *Struct. Chem.*, 32 (2021) 1357-1363.
- [3] L. Martinez, R. Andrade, E.G. Birgin, J.M. Martinez, PACKMOL: a package for building initial configurations for molecular dynamics simulations, *J. Comput. Chem.*, 30 (2009) 2157-2164.
- [4] J. Li, S. Jin, G. Lan, X. Ma, J. Ruan, B. Zhang, S. Chen, L. Li, Morphology control of 3-nitro-1,2,4-triazole-5-one (NTO) by molecular dynamics simulation, *CrystEngComm*, 20 (2018) 6252-6260.
- [5] Q.-K. Li, A. Kutana, E.S. Penev, B.I. Yakobson, Iron corrosion in the “inert” supercritical CO₂, ab initio dynamics insights: How impurities matter, *Matter*, 5 (2022) 751-762.
- [6] X. Zhao, Y. Liu, Origin of Selective Production of Hydrogen Peroxide by Electrochemical Oxygen Reduction, *J. Am. Chem. Soc.*, 143 (2021) 9423-9428.
- [7] J.-P. Ryckaert, G. Ciccotti, H.J.C. Berendsen, Numerical integration of the cartesian equations of motion of a system with constraints: molecular dynamics of n-alkanes, *J. Comput. Phys.*, 23 (1977) 327-341.
- [8] C. Jarzynski, Nonequilibrium Equality for Free Energy Differences, *Phys. Rev. Lett.*, 78 (1997) 2690-2693.
- [9] X. Zhao, Y. Liu, Unveiling the Active Structure of Single Nickel Atom Catalysis: Critical Roles of Charge Capacity and Hydrogen Bonding, *J. Am. Chem. Soc.*, 142 (2020) 5773-5777.
- [10] Y. Qiang, L. Guo, H. Li, X. Lan, Fabrication of environmentally friendly Losartan potassium film for corrosion inhibition of mild steel in HCl medium, *Chem. Eng. J.*, 406 (2021) 126863.

- [11] J.W. Chen, Z. Zhang, H.M. Yan, G.J. Xia, H. Cao, Y.G. Wang, Pseudo-adsorption and long-range redox coupling during oxygen reduction reaction on single atom electrocatalyst, *Nat. Commun.*, 13 (2022) 1734.
- [12] R. Khatiwada, R.A. Root, L. Abrell, R. Sierra-Alvarez, J.A. Field, J. Chorover, Abiotic reduction of insensitive munition compounds by sulfate green rust, *Environ. Chem.*, 15 (2018) 259-266.
- [13] Kien-Yin Lee, L.B. Chapman, M.D. Cobura, 3-Nitro-1,2,4-triazol-5-one, a less sensitive explosive, *J. Energetic Mater.*, 5 (1987) 27-33.
- [14] A. Halasz, J. Hawari, N.N. Perreault, New Insights into the Photochemical Degradation of the Insensitive Munition Formulation IMX-101 in Water, *Environ. Sci. Technol.*, 52 (2018) 589-596.
- [15] N. Bhatnagar, G. Kamath, J.J. Potoff, Prediction of 1-octanol-water and air-water partition coefficients for nitro-aromatic compounds from molecular dynamics simulations, *Phys. Chem. Chem. Phys.*, 15 (2013) 6467-6474.